

CROSS-CALIBRATION OF GNC AND OLA LIDAR SYSTEMS ONBOARD OSIRIS-REX

Jason M. Leonard^{*}, Michael C. Moreau[†], Peter G. Antreasian^{*}, Kenneth M. Getzandanner[†], Estelle Church[‡], Curtis Miller[‡], Michael G. Daly[§], Olivier S. Barnouin[¶], and Dante S. Lauretta[¶]

The Origins, Spectral Interpretation, Resource Identification, and Security–Regolith Explorer (OSIRIS-REx) mission carried two distinct light detection and ranging (LIDAR) systems: A scanning LIDAR called OSIRIS-REx Laser Altimeter (OLA) as part of the science payload, and a flash LIDAR system has part of the Guidance, Navigation, & Control (GNC) subsystem to serve as a navigation sensor during TAG. This presents a unique opportunity to compare the performance of the two LIDAR systems in proximity to a small asteroid body. During the Orbital B mission phase, between June to August 2019, the OSIRIS-REx spacecraft orbited Bennu in a near-circular terminator orbit during which the altitude above the surface varied between 645 m to 740 m. Over a five week period observations were recorded with the OLA instrument that were subsequently used to construct a global digital terrain map (DTM) with a resolution of 5 cm and accuracy of ± 20 cm. This model provides an excellent reference for assessing the performance of the GNC LIDAR system. Two different GNC LIDAR checkout activities were also conducted during the Orbital B phase: A limb-crossing checkout featured a series of slews to collect GNC LIDAR data across varying ranges and phase angles and operate the automatic gain control modes of the device; An OLA-GNC LIDAR cross calibration was designed to collect data from both the OLA and GNC LIDAR devices with overlapping footprints while the spacecraft was pointed nadir. This paper compares the on-orbit performance observed during the cross-calibration activity. The OLA-based global DTM and point clouds are used to evaluate the GNC LIDAR not available during previous analysis. The GNC LIDAR measurements were found to be well within accuracy and precision specified for the instrument, but much noisier than the measurements from OLA within this operating regime.

INTRODUCTION

NASA’s Origins, Spectral Interpretation, Resource Identification, and Security–Regolith Explorer (OSIRIS-REx) is a New Frontiers-class asteroid sample return mission that launched on September 8, 2016. The target for the OSIRIS-REx mission was the 500-m-diameter B-type near-Earth asteroid (101955) Bennu (Figure 1). The primary objective of the mission was to collect a sample from the surface of Bennu and return it to Earth.^{1–3} OSIRIS-REx spent almost two years flying in close proximity to Bennu and mapping it in unprecedented detail in order to aid in selection of a suitable

^{*}KinetX, Inc., Space Navigation and Flight Dynamics Practice, 21 W. Easy St., Suite 108, Simi Valley, CA 93065, USA.

[†]NASA/GSFC Navigation and Mission Design Branch, 8800 Greenbelt Rd, Greenbelt, MD 20771, USA.

[‡]Lockheed Martin Space Systems Company, 12257 South Wadsworth Blvd, Littleton, CO 80125, USA.

[§]The Centre for Research in Earth and Space Science, York University, Toronto, Ontario, Canada.

[¶]The Johns Hopkins University of Applied Physics Laboratory, Laurel, Maryland, USA.

[¶]Lunar and Planetary Laboratory, University of Arizona, 1415 N 6th Ave, Tucson, AZ 85705, USA.

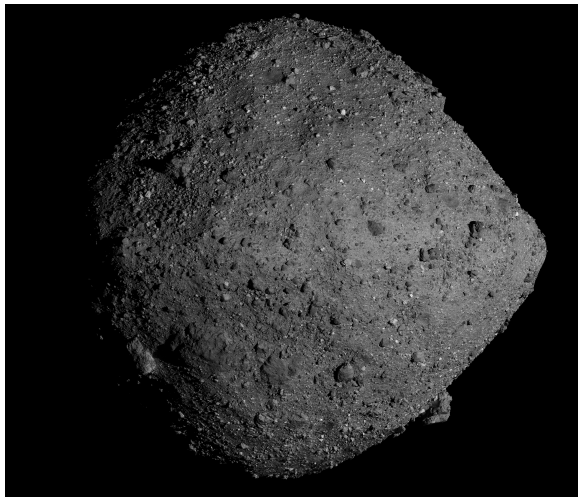


Figure 1: Bennu; the sample collection site Nightingale is visible in the Northern hemisphere.

sample collection site. On October 20, 2020, the spacecraft was navigated to a small crater in the Northern hemisphere of Bennu where the sample was collected in a Touch-and-Go (TAG) maneuver.³ In May 2021 the spacecraft conducted a maneuver to depart Bennu and setup a rendezvous with the Earth on September 24, 2023, when the sample return capsule will enter the Earth’s atmosphere and touch-down within the Utah Test and Training Range, West of Salt Lake City, Utah.

The OSIRIS-REx spacecraft was flown with two light detection and ranging (LIDAR) instrument systems in order to map the entire surface of Bennu and provide navigation updates for the TAG sample collection event. The OSIRIS-REx Laser Altimeter (OLA) is a scanning LIDAR which served as one of the primary science instruments, and was used to measure the range to the surface of Bennu throughout the mission for the purpose of constructing topographic maps.⁴⁻⁷ The Guidance, Navigation, & Control (GNC) LIDAR system consisted two identical flash LIDAR devices (GNC-1 and GNC-2 LIDAR) intended to provide a primary and redundant measurement source for onboard navigation during TAG.⁸⁻¹⁰ The unexpectedly rough and hazardous surface of Bennu ultimately required a more robust image-based onboard navigation method;^{3,11,12} therefore, use of the GNC LIDAR during the mission was limited to the checkout activities described in this manuscript.

Two distinct flight activities were conducted during the Orbital B mission phase with the objective to assess the performance of the GNC LIDAR sensor.³ A limb-crossing calibration activity involved slewing the spacecraft such that the GNC LIDAR ground track swept across the asteroid simulating the limb crossings and changes in ranges and incident angles that would be experienced during TAG. A separate cross-calibration activity was conducted to perform a cross-comparison between the OLA and GNC LIDAR devices using more benign ranging geometries. During this activity, GNC LIDAR observations occurred at nadir-point in between OLA lasing periods, and included optical navigation (OpNav) images collected before and after by the NavCam 1 imager (Reference 13) for context. Both the limb-crossing and cross-calibration checkout activities were repeated twice: once with GNC-1 LIDAR and again with GNC-2 LIDAR. OLA observations were collected throughout the mission to construct global and local topographic maps of Bennu and to aid in selection of a suitable sample collection site; the OLA Low-Energy Laser Transmitter (LELT) system mapped the entire surface of Bennu with a resolution of 5 cm and an accuracy of better than ± 20 cm.⁶ The shape model published in Reference 6, known as OLA v20, was the precursor to the one used in this work, OLA v21. OLA v21 incorporated minor corrections made to the OLA v20 data.

This paper compares the on-orbit performance observed with the GNC LIDAR to the OLA observations and high resolution OLA v21 shape model, primarily focusing on the observations recorded from the OLA-GNC LIDAR cross calibration activity. Reference 14 provides a preliminary analysis of observations recorded during the GNC LIDAR limb-crossing calibration; however, the final OLA-based shape model was not available at the time analysis was conducted. In this paper, GNC LIDAR observations will be compared to the global OLA-derived shape model, and direct comparisons will be made between observations from the GNC LIDAR and OLA where possible. Biases between OLA and the GNC LIDARs are also estimated in order to improve the understanding of the differences between OLA and the GNC LIDARs. Data quality is re-assessed with these updated models in order to provide an improved metric of the quality of the GNC LIDAR.

LIDAR INSTRUMENTS BACKGROUND

Reference 15 provides a useful overview of different LIDAR sensors and some of their applications for spacecraft relative navigation. Scanning LIDAR sensors use a narrow laser beam that is swept over the sensor Field of View (FOV) to obtain range measurements to objects within the scene. The laser direction is changed by a set of mirrors, lenses, and/or other devices, and the return signal typically illuminates a single detector. By combining knowledge of the laser direction and the measured time delay of the returned signal, a three-dimensional (3D) point cloud of the scene may be constructed. A flash LIDAR illuminates the entire scene at once and the returned signal illuminates a detector array. The device measures the time delay between the pulse or “flash” from the laser and the detection of the return signal at each detector pixel. Since each pixel location maps directly to a known line-of-sight direction a 3D point cloud of the scene can be constructed using the range measurements from each pixel. The OSIRIS-REx mission is unique in that it flew both flash and scanning LIDAR systems, each with differing operational objectives and performance. This provides a unique opportunity to characterize the performance of these different sensors in flight.

OLA (Figure 2) was contributed to the OSIRIS-REx mission by the Canadian Space Agency (CSA) in order to measure the range between the spacecraft and the surface of Bennu; observations from OLA have enabled the creation of digital terrain maps (DTMs) of unprecedented spatial scales for a planetary mission.⁷ OLA is a two-dimensional scanning LIDAR with two laser emitters

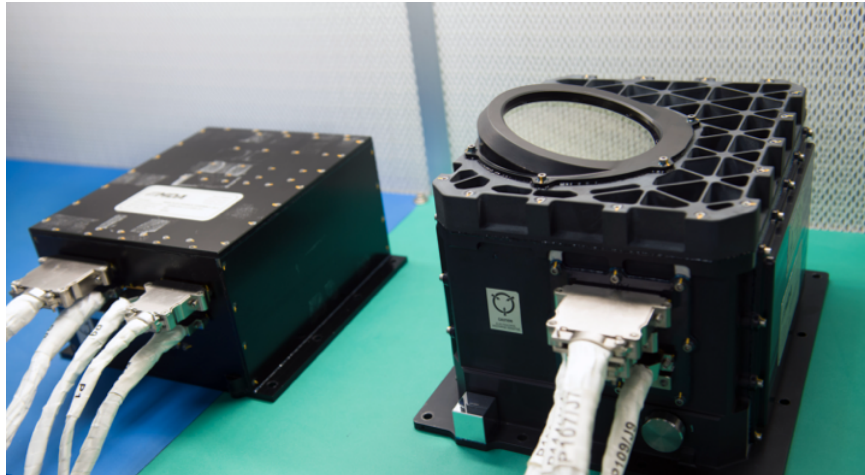


Figure 2: The OSIRIS-REx Laser Altimeter (OLA), a contributed instrument from the Canadian Space Agency, consists of the electronics unit (left) and the optical head unit (right).⁴

and operational modes optimized for different ranging distances: a high-energy mode known as High-Energy Laser Transmitter (HELT) used for ranging from 1-7.5 km at a data rate of 100 Hz; and a low-energy but high data-rate (10 kHz) mode known as LE LT, used for rapid ranging and LIDAR imaging at 500 m to 1 km. The LE LT mode was used exclusively for the global DTM data collection campaign during the Orbital B mission phase in July–August 2019, as well as for the cross-calibration flight activity.

Table 1: OLA Performance Requirements.

Mission Phase	Range to Surface [m]	Range Accuracy [cm]	Range Precision [cm]
Preliminary Survey	6750	50	30
Detailed Survey	4750	50	30
Orbital A	1250	50	30
Orbital B	750	30	13
Reconnaissance	500	30	4

The OLA instrument is a hybrid of the flight-proven scanning lidar instruments on the XSS-11¹⁶ and Phoenix Mars Lander¹⁷ missions. In the OLA design, the same detector assembly is used to receive signals from either laser. The optical pulse triggers a timing circuit that generates the “zero-time” reference. This pulse reflects off a steering mirror. The back-scattered signal reflects from the scanning mirror and is focused by an off-axis parabolic reflector to the receiver’s silicon avalanche photodetector. The time of the received pulse is determined relative to the “zero-time” reference; the pulse time-of-flight determines the distance. Each pulse provides range, azimuth, elevation, and received signal intensity information and time tag. The ranging performance requirements levied on the OLA system are summarized in Table 1.

The OSIRIS-REx GNC LIDAR instrument (Figure 3) is a flash LIDAR that was built by Advanced Scientific Concepts (ASC) to meet specific requirements outlined by Lockheed Martin for



Figure 3: The Advanced Scientific Concepts GoldenEye 3D Flash LIDAR flown as the OSIRIS-REx GNC LIDAR.

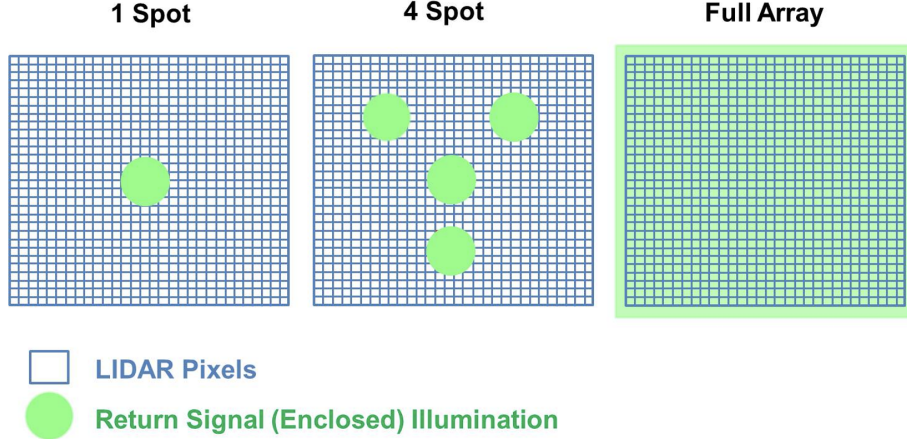


Figure 4: GNC LIDAR DOE settings and corresponding detector illumination modes. Observations discussed in this paper were collected in the 1 Spot mode.

use as a navigation sensor for the autonomous navigation update during TAG.^{9,14} The GNC LIDAR is a 128x128 pixel, 6 degree FOV range-finder with three Diffractive Optical Element (DOE) configurations (Figure 4) that allow an operational range between 2.8 and 1000 meters. At the closest ranges the “Full Array” DOE setting spreads the returned energy across the entire 128x128 pixel array. At the furthest ranges, the “1 Spot” DOE setting allows backscatter signals to pass through the diffuser with no diffraction, illuminating a narrow grid of pixels near the center of the detector array. For intermediate ranges, the “4 Spot” DOE setting causes the returned laser energy to be projected on four separate spots across the detector.⁹

The GNC LIDAR has both a manual and software driven automatic mode known as Automatic Gain Control (AGC). In manual mode the LIDAR DOE can be configured as well as the gain of the sensor. AGC mode is driven by the number of illuminated sensor pixels and their intensities. The input feeds a configurable algorithm that adjusts the LIDAR parameters in order to optimize the performance of the system. The TAG sequence was designed to utilize the AGC mode starting with a limb crossing and 1 Spot mode. The GNC LIDAR then automatically transitions the gains and DOE settings as the sensor approaches the surface.

Table 2: GNC LIDAR Performance Requirements.

Range Measurement Accuracy - cluster of no more than 16 pixels	
Range Mean Error	10 cm + 1% of range, 3 sigma
Range Variation	10 cm + 1% of range, 3 sigma

During the LIDAR checkouts conducted in the Orbital B mission phase, the spacecraft’s true range to the surface varied between 645 m to 740 m. Measured ranges were expected to be as high as 850 meters during the extremes of limb crossing slews. Consequently, the LIDAR was operated in the 1 Spot (no diffraction) mode with fixed gain settings. Performance requirements levied on the device in order to meet the anticipated requirements for TAG navigation updates are summarized in Table 2. As an example, for a distance to the surface of 650 meters (minimum expected during cross-calibration activities) the corresponding range accuracy requirement is 6.6 meters. At a distance of 100 m above the surface the ranging accuracy required is 1.1 m.

The ASC flash LIDAR flown on OSIRIS-REx has heritage from the DragonEye sensor, selected by SpaceX as the primary rendezvous sensor for the first flights of the Dragon Commercial Cargo vehicle. A DragonEye prototype flew on two Space Shuttle Missions, STS-127 and STS-133, and was the first example of a flash LIDAR system used for spacecraft relative navigation.¹⁵ The NASA Engineering and Safety Center (NESC) commissioned a report that detailed the performance of the DragonEye flight tests, as well as other LIDAR flight demonstrations conducted in that timeframe.¹⁸

FLIGHT ACTIVITIES

Three different types of checkout activities were conducted with the GNC LIDARs during the OSIRIS-REx mission to monitor functional status and assess performance: Routine functional checkouts performed during outbound cruise to Bennu, an asteroid limb crossing checkout to mimic changing ranges and incidence angles that would be experienced during TAG, and a cross calibration checkout designed to collect data coincident with the OLA and navigation cameras.

Cruise Checkouts

Following launch, both GNC LIDARs were operated approximately every six months to evaluate and trend health. As no ranging target was available, the cruise checkouts were limited to evaluating the sensor, the ARC (Automatic Range Correction) pixels, temperatures and the laser properties.¹⁴

Limb-Crossing Checkout

The limb-crossing checkout was the first GNC LIDAR flight activity to range to the surface of Bennu, conducted during the Orbital B phase in June 2019. Beyond providing the first confirmation of ranging performance at Bennu, this activity was specifically designed to assess the performance of both GNC-1 and GNC-2 LIDAR over some of the variations in range and incidence angle that would be experienced during the TAG event. The attitude profile during TAG sweeps the GNC LIDAR footprint off the limb of Bennu during one attitude transition, thus this checkout was designed to provide multiple limb-crossing data points. Each sequence in the limb-crossing checkout began with the spacecraft pointing nadir to conduct ten minutes of ranging with Automatic Gain Control activated at low incidence angles. Following the nadir-pointed period, the spacecraft is commanded to slew through an angle of approximately 24 degrees, taking the GNC LIDAR ground track fully off the limb of Bennu. The slew was then reversed to cross through nadir and cross the opposite limb of Bennu. The cross-asteroid scans are repeated a total of six times before returning to nadir, after which the GNC LIDAR is commanded to standby. Full slews took on the order of 160 seconds to complete. The activity described above was repeated a total of five times over the course of one day starting June 15, 2019 using GNC-1 LIDAR. The entire activity was then repeated on June 16, 2019 with GNC-2 LIDAR.

The spacecraft altitude varied between 645 to 740 m during the checkouts. The scans allowed data to be collected over a wide range of incidence angles and limb crossings. During the slews, range measurements were expected to vary between approximately 650 to 850 m. Repeating the scanning activity multiple times for several hours allowed data to be collected over a range of Bennu latitudes and altitudes from the surface as the spacecraft progressed through its orbit about Bennu.

The GNC LIDAR was operated in its automatic gain control mode, with gain initially set to 0 in the nadir attitude, with alternating downlink of full frame images at 0.1 Hz and 40x40 windowed images at 2 Hz. Before initiating slews the GNC LIDAR was reconfigured with an initial gain

of 15, and to downlink 40x40 pixel images at 2 Hz. Preliminary results from the GNC LIDAR Limb-Crossing Checkout were described by Reference 14.

OLA-GNC LIDAR Cross Calibration

The OLA-GNC LIDAR Cross Calibration was designed to perform a more precise characterization of GNC LIDAR ranging performance while ranging in a nadir attitude, while also collecting data with the OLA for cross comparison. OLA provides extremely precise ranging measurements in the Orbital B flight regime (at distances approaching one kilometer from the surface), whereas the GNC LIDAR is approaching the limit of its operational range at these distances. OLA thus provides a good reference for assessing the GNC LIDAR performance at these distances. Moreover, the post processing of OLA and Optical Navigation (OpNav) measurements, in conjunction with the global shape model derived from OLA measurements provides a means to develop a highly accurate reference ephemeris for post-processing of the GNC LIDAR measurements.

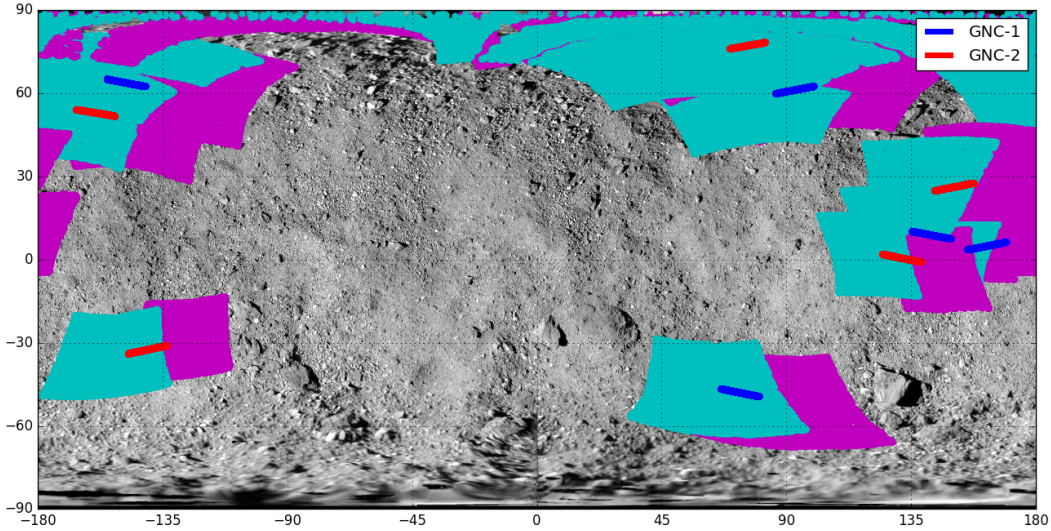


Figure 5: GNC LIDAR Cross Calibration surface intercept locations with OLA scan footprints prior to (magenta) and after (cyan) their respective GNC LIDAR footprints.

Since OLA and GNC LIDAR cannot be operated simultaneously, this checkout was designed to alternate measurements between the two ranging devices such that the ground tracks overlap. OLA creates a scan pattern covering ± 5 deg in each axis. The GNC LIDAR beamwidth when operating in the 1 Spot mode with a 32x32 detector pixel range, creates on average a 10x16 m footprint on the surface of Bennu during the checkout. The GNC LIDAR images taken during the cross calibration generally had valid returned ranges only on a 6x6 pixel subgrid of the 32x32 detector range. This 6x6 subgrid creates a footprint of about 2x2 meters for a single image at the operating altitudes of the cross calibration activity where the range to the surface varied between 645 m to 740 m. OLA scans were planned to be 17.9 minutes start-to-start with 5.4 minute lasing periods (spaced by 12.5 minutes). GNC LIDAR scans were planned to be approximately 12 minutes in length in between OLA lasing periods. This schedule allows the ground track of subsequent OLA scans to overlap each other, and for all of the GNC LIDAR scans to overlap areas in which OLA ranges are available. NavCam 1 images were taken at the beginning and end of the GNC LIDAR ranging sequences to aid in creating an independent reconstruction of the spacecraft trajectory during the

cross-calibration activity. Figure 5 shows the OLA scan footprint prior to (magenta) and after (cyan) their respective GNC LIDAR footprints for the cross-calibration activity.

The GNC LIDAR was operated in its AGC mode with gain initially set to 0. A 32x32 pixel range image was recorded at 10 Hz rate. Twelve-minute ranging periods were repeated five times with GNC-1 LIDAR on July 6, 2019, and five more times with GNC-2 LIDAR on August 2, 2019 for a total of 60 minutes of ranging data on each of these days.

LIDAR MEASUREMENT MODELING

In order to be consistent with the optical image measurement processing, the LIDAR measurements are computed in the barycentric dynamical time (TDB) space-time reference frame with the origin as the Solar System Barycenter (SSB). The spacecraft ephemeris as well as Bennu have all been estimated in this reference frame through radio metric data as well as OpNavs.^{19,20} A single LIDAR return can be modeled as half the duration between the return detection time (t_d) and the emission time (t_e) measured by the onboard LIDAR clock/oscillator. During this duration, the onboard clock/oscillator can drift relative to the coordinate reference time. In addition, there could be a constant bias on the returned values. The fidelity of each model is presented for completeness and can be modified for the desired application and major error sources.

The two models for processing LIDAR data analyzed in this work are the Ray-Traced Surface Intercept Model, and the Point Cloud Projection model. The Ray-Traced Surface Intercept Model requires an underlying shape model or DTM of the terrain in order to compute a LIDAR measurement to process the observed values. The Point Cloud Projection model does not need a shape model or DTM and simply uses the observed range to project the intercept point onto the surface of the body.

Ray-Traced Surface Intercept Model

The following is the mathematical implementation of a single LIDAR return intercept location of a surface model such as a DTM. The model assumes that t_e is known, though it can be similarly solved for if t_d is known. The computed LIDAR range, ρ , is calculated as half the total round-trip delay as

$$\rho = \frac{1}{2} (\tau_d + \tau_u + \delta_{clock}) + b_L, \quad (1)$$

where τ_d is the down-leg light time from the LIDAR to the surface, τ_u is the up-leg light time from the surface to the detector, δ_{clock} is the delay due to the difference in time due to clock drift, and b_L is the bias in the instrument. The down-leg light time is computed as the difference in the time-of-intercept (t_i) and t_e as

$$\tau_d = (t_i - t_e) = \frac{1}{c} \hat{n}^T (\mathbf{S}(t_i) - \mathbf{L}(t_e)), \quad (2)$$

where c is the speed of light, \hat{n} is the surface normal vector of the photon intercept point on the model, \hat{u} is the LIDAR shot direction, $\mathbf{S}(t_i)$ is the intercept point at t_i , and $\mathbf{L}(t_e)$ is the location of the LIDAR at t_e . The location of the LIDAR in the shape-model reference frame (A-Frame) must be computed to determine the body-centric ray-trace surface intercept location, \mathbf{X}_i , as

$$\mathbf{L}(t_n) = T_B^A(t_i) T_N^B(t_e) (\mathbf{R}_b(t_e) + \mathbf{R}_{s/c}(t_e) + T_S^N(t_e) \mathbf{R}_L), \quad (3)$$

where $\mathbf{R}_b(t_e)$ is the location of the center-of-mass of the intercepted body at time t_e relative to the SSB, $\mathbf{R}_{s/c}(t_e)$ is the location of the center-of-mass of the spacecraft relative to the intercepted body center-of-mass at t_e , \mathbf{R}_L is the location of the LIDAR detector relative to the spacecrafats center-of-mass, $T_S^N(t_e)$ is the transformation from the spacecraft reference frame (S-Frame) to the inertial reference frame (N-Frame), $T_N^B(t_e)$ is the transformation from the N-Frame to the intercepted body's principal-axis body-fixed reference frame (B-Frame) at t_e , and $T_B^A(t_i)$ is the transformation from the B-Frame to the shape model or DTM reference frame (A-Frame).

The LIDAR direction vector, \hat{u}_L , in the local LIDAR reference frame (L-Frame) must be transformed to \hat{u} (A-Frame) to compute the surface intercept location. The model implemented in this work corrects the incoming/outgoing LIDAR photon direction detected by the instrument for aberration by

$$\hat{u}_N = T_L^N \hat{u}_L, \quad (4)$$

$$\hat{u} = T_B^A(t_i) T_N^B(t_e) f_{abb}(\hat{u}_N, \mathbf{V}_L), \quad (5)$$

where \mathbf{V}_L is the velocity of the LIDAR relative to the coordinate center of the N-Frame (SSB). The aberration is computed via the function $f_{abb}(\hat{u}_N, \bar{\mathbf{V}}_L)$ which can either be the Newtonian or relativistic correction.^{21,22}

Since t_i is unknown, it must be solved for through an iterative process to determine the down-leg light time. \mathbf{X}_i is determined by solving the following equation for $\mathbf{S}(t_i)$

$$\mathbf{S}(t_i) = \sigma \mathbf{X}_i + T_B^A(t_i) (\mathbf{R}_{CF} + T_N^B(t_i) \mathbf{R}_b(t_i)), \quad (6)$$

where σ is the shape scale factor to account for any global size error in the shape model or DTM, \mathbf{R}_{CF} is the center-of-mass to center-of-figure offset of the intercepted body, and \mathbf{R}_b is the position of the body relative to the inertial reference system (SSB).

Once the down-leg light time is known, the up-leg light time can be computed as

$$\tau_u = (t_d - t_i) = \frac{\|\mathbf{L}(t_d) - \mathbf{S}(t_i)\|}{c}, \quad (7)$$

where $\mathbf{L}(t_d)$ is computed by replacing t_e with t_d in Eq. 3. Similar to the down-leg light time, the up-leg light time must be iteratively solved for to determine t_d .

If the LIDAR clock/oscillator has not been calibrated to report durations in the desired space-time reference frame or a significant drift in the clock is possible, the additional delay due to this clock drift, δ_{clock} , can be computed as a polynomial in time (see Reference 23) by

$$t_{clock} - t_{s/c} = a(t_{s/c} - t_{ref})^2 + b(t_{s/c} - t_{ref}) + c, \quad (8)$$

$$\delta_{clock} = (t_{s/c} - t_{clock})_{t_d} - (t_{clock} - t_{s/c})_{t_e}, \quad (9)$$

where a , b , and c are the polynomial clock model quadratic, linear, and constant terms, t_{clock} is the epoch that the LIDAR measured, $t_{s/c}$ is the local time on the spacecraft, t_{ref} is the reference epoch of the drifting clock, and $(\dots)_{t_d}$ means the drift was evaluated at t_d and $(\dots)_{t_e}$ at t_e . At this point, depending on the fidelity needed, the epoch $t_{s/c}$ can be converted to the appropriate space-time reference frame if $t_{s/c}$ is not modeled as TDB.²⁴ While b_L is modeled as a constant bias in the LIDAR, δ_{clock} is a function of the total light time, $\tau_d + \tau_u$, and thus changes for varying ranges.

Point Cloud Projection

Generating LIDAR point clouds around planetary bodies has been used for a variety of analysis.^{25–27} The operational model implemented in the OD software used in this analysis is consistent with the Ray-Traced Surface Intercept Model described previously and is performed in the TDB space-time reference frame. Reference 27 describes four methods to produce point clouds of varying fidelity around planetary bodies of which the pointing aberration model and special relativity model are similar to what is implemented in the OD software.

A model for the observed range value output by the OLA and GNC LIDAR instruments is given in Eq. 1. The round-trip light time in the TDB frame is thus

$$RTLT = \tau_d + \tau_u. \quad (10)$$

The position of the LIDAR is computed at the time of emission as given by Eq. 3. The outgoing LIDAR shot direction is corrected for aberration as in Eq. 5. The initial guess of the LIDAR intercept point is computed using Eq. 20 in Reference 27. The down-leg and up-leg light time solutions are solved for without assuming a constant velocity assumption as is done in Reference 27. Once the down-leg light time is known, the intercept location is simply

$$\mathbf{S}(t_i) = \tau_d \hat{\mathbf{u}} + \mathbf{L}(t_e). \quad (11)$$

Shape Model

During a five-week period in 2019, the OLA instrument mapped the surface of Bennu during the Orbital B mission phase, as the spacecraft orbited Bennu in a near-circular terminator orbit with a radius of approximately 1 km. The overlapping scans of Bennu combined with the instrument’s high measurement rate (10 kHz) resulted in average spot spacings below 5 cm globally, other than in areas where shadowing prevented measurement. Point clouds derived from these measurements were used to construct a global DTM with facet vertex separations of ≈ 20 cm that visually compare well with corresponding imagery of Bennu. Assessments that include detailed optical navigation efforts, adoption of absolute OLA ranges, and updated estimates of the asteroid GM indicate that the accuracy of the OLA global DTM is better than ± 20 cm.²⁸ The precision of the global DTM, based on differences between overlapping OLA scans, is on the order of ± 1.25 cm.⁶ The OLA v20 model described in Reference 6 is currently available via the Small Body Mapping Tool* with the intention of making the OLA v21 model used in this work available.

RESULTS

An OD solution for the OSIRIS-REx spacecraft was estimated for data between June 28, 2019 and August 5, 2019 in the Orbital B time-frame. Radio metric Doppler data, OLA data, as well as optical images based on the shape model maplets with a resolution of 15 cm/px were used to fit a consistent trajectory over the data span. Doppler was collected during tracking passes roughly 3 times a day over this time-frame. OLA scans were executed multiple times a day throughout all of Orbital B in order to build the high resolution shape model. The OLA and GNC LIDAR data taken during the OLA GNC calibration was not used in the OD solution. OpNav images were taken every 2 hours between HGA passes from roughly 22:30 to 13:30 the following day.

*<https://sbmt.jhuapl.edu>

The estimated parameters included spacecraft related force model parameters of a constant solar radiation pressure (SRP) scale factor, desaturation maneuvers, stochastic accelerations, and stochastic OpNav pointing corrections (applied only when OpNav image pointing was not corrected *a priori* using stellar images). A center-of-figure to center-of-mass offset was estimated for the shape model of Bennu as well as a constant frame offset between the shape model and the rotation state of Bennu. The frame offset of the shape model relative to the principal axis frame was estimated as a 321 Yaw-Pitch-Roll correction of 0.0 mdeg, 24.7 mdeg, and -5.2 mdeg, respectively. The principal axis rotation state as well as the GM of Bennu were also estimated. The Bennu ephemeris was not estimated as an independent solution applicable to this time period was used.²⁹ The OD solution provided a long baseline fit of the spacecraft trajectory as well as a refined estimate of the orientation of Bennu relative to inertial space to allow for accurate pre-registration of the OLA and GNC LIDAR data for the OLA GNC LIDAR checkout.

Three types of data were acquired from the GNC LIDAR during the OLA-GNC LIDAR Cross Calibration. Raw flash LIDAR images were taken at 10 Hz over the 32x32 pixel grid. From the raw images, an un-filtered range value was computed as the average range over all returns in the 32x32 pixel grid that are above an intensity threshold of 500. This un-filtered range value was then filtered using a running mean. The filtered range returns are not analyzed in this work. The un-filtered range observables are used along with the ray-traced surface intercept model while the raw images are used with both the ray-traced surface intercept model and the point cloud projection algorithm.

The OD trajectory was used to generate residuals based on the un-filtered and raw images. Both computation models were used to do pre-registration analysis of the telemetry based un-filtered GNC LIDAR data as well as using the individual raw images taken during the cross calibration activity to assess the performance of the two GNC LIDARs. Evaluation of the pre-registration allowed for an initial glimpse into the performance of the GNC LIDAR vs. OLA in the overlapping regions as well as to assess any initial pointing error or biases seen in the instruments themselves. The pre-registration ray-traced intercept residuals were fit to the OLA DTMs and GNC LIDAR pointclouds to overlapping OLA point-clouds and DTMs to assess the GNC LIDAR performance.

Pre-registration of un-filtered GNC LIDAR

Five individual sub-scans were recorded for both GNC-1 and GNC-2 LIDARs each providing valid ranges for 10 minutes in duration during the OLA GNC LIDAR checkout. Each LIDAR maintained an unfiltered and filtered (running mean) telemetry channel. The un-filtered data was used with the ray-trace algorithm using the v21 DTMs to compute the intercept point. A wide variety of regions were covered during the OLA-GNC LIDAR cross calibration as shown in Figure 5. The precision of the instrument and pre-registration terrain mismatch errors can clearly be seen in Figure 6. Figures 6a through 6e display the prefit results for the GNC-1 LIDAR while Figures 6f through 6j show the results for GNC-2 LIDAR. The GNC-2 LIDAR instrument exhibits a frequent range jump throughout each of the five sub-scans of 2.9 meters. A 2.9 meter error equates to a 19.3 nsec error in the round-trip light time. This 2.9 meter jump is consistently produced throughout the pass over a wider range of returned intensities and is always producing an observed range longer than the actual range to the surface. During the calibration activity, GNC-1 LIDAR did not experience any range jumps in the observables.

A major issue with the un-filtered data when attempting to fit the ray-traced and point-cloud models is that the pixels of which the observed values were averaged over are not known as the telemetry channel just reports the observed range-to-surface. The center pixel of the 32x32 sub-grid

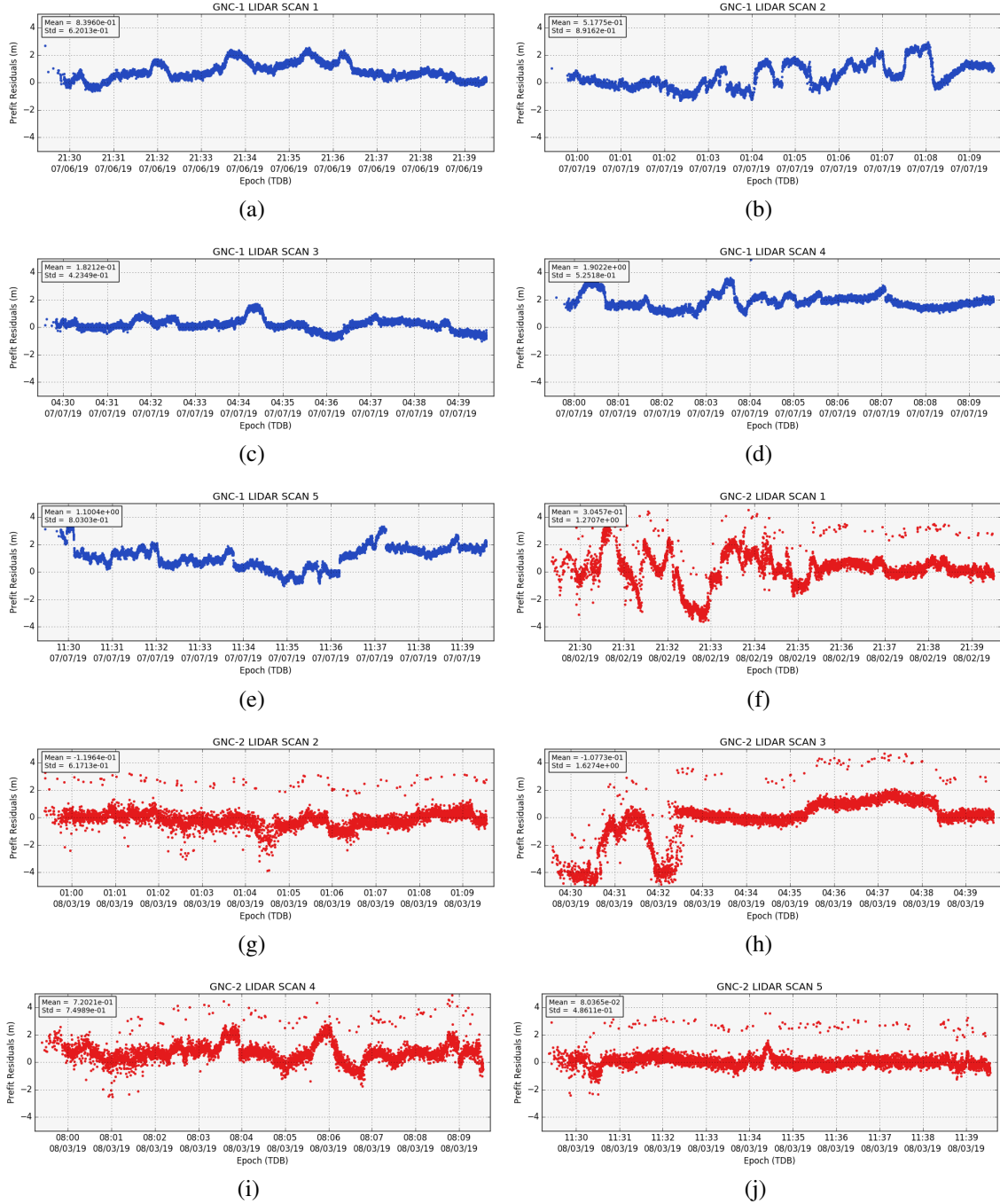


Figure 6: Un-filtered GNC LIDAR prefit residuals using the ray-traced surface intercept model.

is used as the boresight of the returned range. When attempting to fit the data, a constant pointing correction is needed to adjust the scan to the appropriate terrain on the surface but using the 32x32 sub-grid center provides a close-enough pre-registration.

The mean and standard deviation (SD) of each sub-scan is provided in Figure 6. If all of the structure in the residuals is assumed to be terrain error, filtering the data with a running mean or another variation of a low-pass filter can remove the terrain error and allow for a better understanding

Table 3: GNC LIDAR precision.

Instrument	Scan 1 SD (m)	Scan 2 SD (m)	Scan 3 SD (m)	Scan 4 SD (m)	Scan 5 SD (m)
GNC-1	0.61	0.88	0.41	0.51	0.79
GNC-2	1.17	0.41	1.54	0.60	0.26

of the precision of the instrument itself. Table 3 gives the SD of the instruments for each scan using a Savitzky-Golay filter (Reference 30; cubic polynomial over 51 points) to remove the structure in the residuals seen in Figure 6. After filtering the data, the precision of the GNC-1 LIDAR data was less than 0.9 m 1-sigma across the five observing periods while the GNC-2 LIDAR 2 data precision was less than 1.6 m 1-sigma.

Pre-registration of GNC LIDAR Raw Image Point Clouds

The DTMs used in this work were based on OLA scans throughout the Orbital B time-frame to build the global shape model. The individual OLA scans in the OLA GNC LIDAR checkout should match the known terrain of the model well except for known biases in the OLA instrument itself. The shape model reference frame was adjusted relative to the true principal-axis of Bennu from the OD solution to provide a consistent model of any errors in the shape model orientation and center-of-figure to center-of-mass offsets relative to the known inertial orientation of the landmarks from the OpNav images. This consistent reference frame was used throughout the projection of the OLA and GNC LIDAR point clouds.

The pre-registration projection of the OLA point clouds matched the underlying DTMs to within 10 cm for every OLA scan generated in the OLA GNC LIDAR checkout. Figures 7 through 9 show the OLA point clouds before (magenta) and after (cyan) the GNC-1 (blue) and GNC-2 (red) LIDAR raw images. The underlying DTM from the shape model is shown in grey. Each pair of OLA point clouds overlapped at least a portion of the GNC LIDAR raw images. The consistency of the OLA pre-registration projection of the point cloud with the DTMs is shown in Figure 7a, 8a, and 9a.

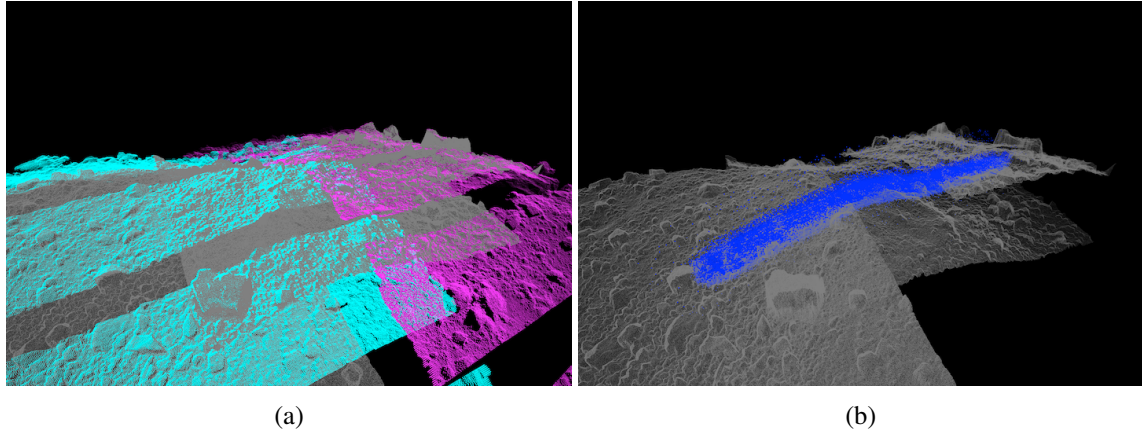


Figure 7: Overlapping OLA scans vs. GNC LIDAR for GNC-1 Scan 5. The underlying DTM (grey) compared to: (a) OLA Scan 1 (magenta) and OLA Scan 2 (cyan); and (b) GNC-1 LIDAR (blue). The same view is provided in both (a) and (b).

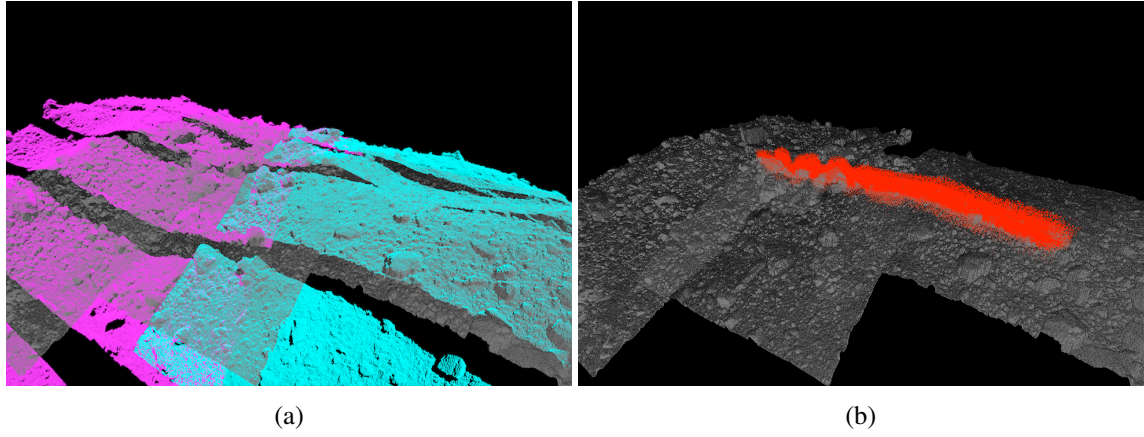


Figure 8: Overlapping OLA scans vs. GNC LIDAR for GNC-2 Scan 1. The underlying DTM (grey) compared to: (a) OLA Scan 1 (magenta) and OLA Scan 2 (cyan); and (b) GNC-2 LIDAR (red). The same view is provided in both (a) and (b).

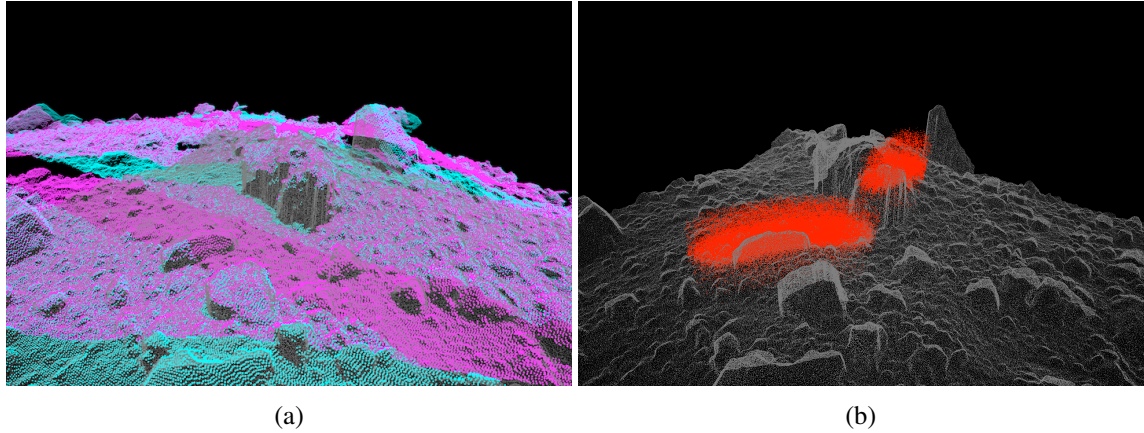


Figure 9: Overlapping OLA scans vs. GNC LIDAR for GNC-2 Scan 3. The underlying DTM (grey) compared to: (a) OLA Scan 1 (magenta) and OLA Scan 2 (cyan); and (b) GNC-2 LIDAR (red). The same view is provided in both (a) and (b).

An individual raw image from the GNC LIDAR spans approximately a 2x2 meter grid on the surface during the cross calibration activity. For each scan, all images taken at 10 Hz with valid range returns were processed obtaining footprints on the surface varying between 20 m to 70 m in length. Figures 7a and 8a are approximately 2x70 m footprints while Figure 9a is approximately a 2x20 m footprint.

Figure 7b shows the GNC-1 LIDAR raw image data for the fifth scan that is of the same terrain as Figure 6e. The random noise of the raw image data is considerably more than that of the underlying DTM terrain as well as the overlapping OLA scans of the same region. Of note is that the raw image data over a short period cannot distinguish small rocks or variations in the terrain. However, over a long enough scan, the data matches the long scale variation in the overall shape of Bennu allowing the data to be distinguished from surrounding terrain.

While several of the GNC LIDAR raw image data traversed relatively flat terrain with smaller rocks, a few of the passes captured large features in their footprints. Figures 8b (GNC-2 LIDAR for

Scan 1) and 9b (GNC-2 LIDAR for Scan 3) are two such instances in which local distinguishable features on a smaller footprint exist. The GNC-2 LIDAR raw image footprint shown in Figure 8b traverses several 3 meter tall features before progressing over smoother terrain. For the third scan of GNC-2 LIDAR, a large feature of 5 meters was detected as seen in Figure 9b.

The pre-registration projection of the point clouds for all of the scans in both GNC LIDARs showed a unique match to the underlying terrain. Of note is the significant level of noise seen in the projection of the point clouds. No reduction of the input data was made based on the returned intensity other than the pixel in the detector had a returned range. Significant outliers were removed from the point clouds that were well outside of the underlying terrain.

Registration of GNC LIDAR Raw Image Point Clouds

Due to the noise level of the pre-registered point clouds produced by the GNC LIDAR raw images, an L1 distance norm weighted point-to-plane Iterative Closest Point (ICP) method (Reference 31) was used to fit the point clouds to the underlying OLA overlapping scans as well as the underlying DTM. Since the OLA point-clouds matched the underlying DTM with minimal adjustment (< 10 cm), a point-cloud sampling of the DTM was used to fill in the gaps where the overlapping OLA point-clouds had no data to compare to the GNC LIDAR. A voxel grid of 10 cm was used to resample the underlying OLA/DTM point cloud producing a point cloud resolution of 10 cm. The GNC LIDAR point cloud was cleaned up to remove any outliers greater than 5 meters and to remove any statistical outliers whose 20 nearest neighbors distances produced a point greater than 3 sigma away. The point clouds were iterated until the point-to-plane distance was minimized. The largest translation corrections were only on the order of 10's of cm showing that that pre-registered projection of the GNC LIDAR point clouds closely matched the surrounding terrain well.

As a metric of the goodness of fit, the absolute point-to-plane distances were computed between the GNC LIDARs and the OLA based terrain. Figure 10 shows this error for the five scans of GNC-1 LIDAR and Figure 11 for the five scans of GNC-2 LIDAR. Not directly shown are the fitted returns that lie underneath the surface of the terrain. Of note is that a majority of the larger residuals and outliers (> 1.5 m) in the data are skewed to reside above the surface while the number of large residuals below are greatly reduced except for the 2.9 meter range jumps. Large scale unique terrain variations can be seen in Figure 10 where the data accurately fits the underlying model. The GNC-1 LIDAR scans had minimal unique features within the LIDAR footprint itself, though a few large rocks or features can be seen to match the point cloud accurately in Figures 10b and 10c.

Closer cross-sections of the absolute point-to-plane distance errors for GNC-2 LIDAR are shown in Figure 11. The most unique large scale feature variations in this data set were seen in Scan 1 (Figure 11a) and Scan 3 (Figure 11c). These unique terrain features allowed for accurate fits of the single raw image where as other scans needed much longer swaths of the LIDAR footprint to be able to fit to the surface variation. The 2.9 meter range jump can be seen in Figures 11a, 11c (below the underlying grey mesh), and 11e. This range jump occurs over the full detector in a single raw image and is not localized to specific pixels within the detector.

Once the GNC LIDAR raw image point clouds were registered to the underlying terrain, the OD process estimated per-scan GNC LIDAR range biases and boresight pointing corrections. A consistent error in the GNC LIDAR boresight was estimated to be less than 10 mdeg. Structure in the range residuals was not improved much over the pre-registration as seen in Figure 6 and estimated range biases consistent with those reported in Figure 6.

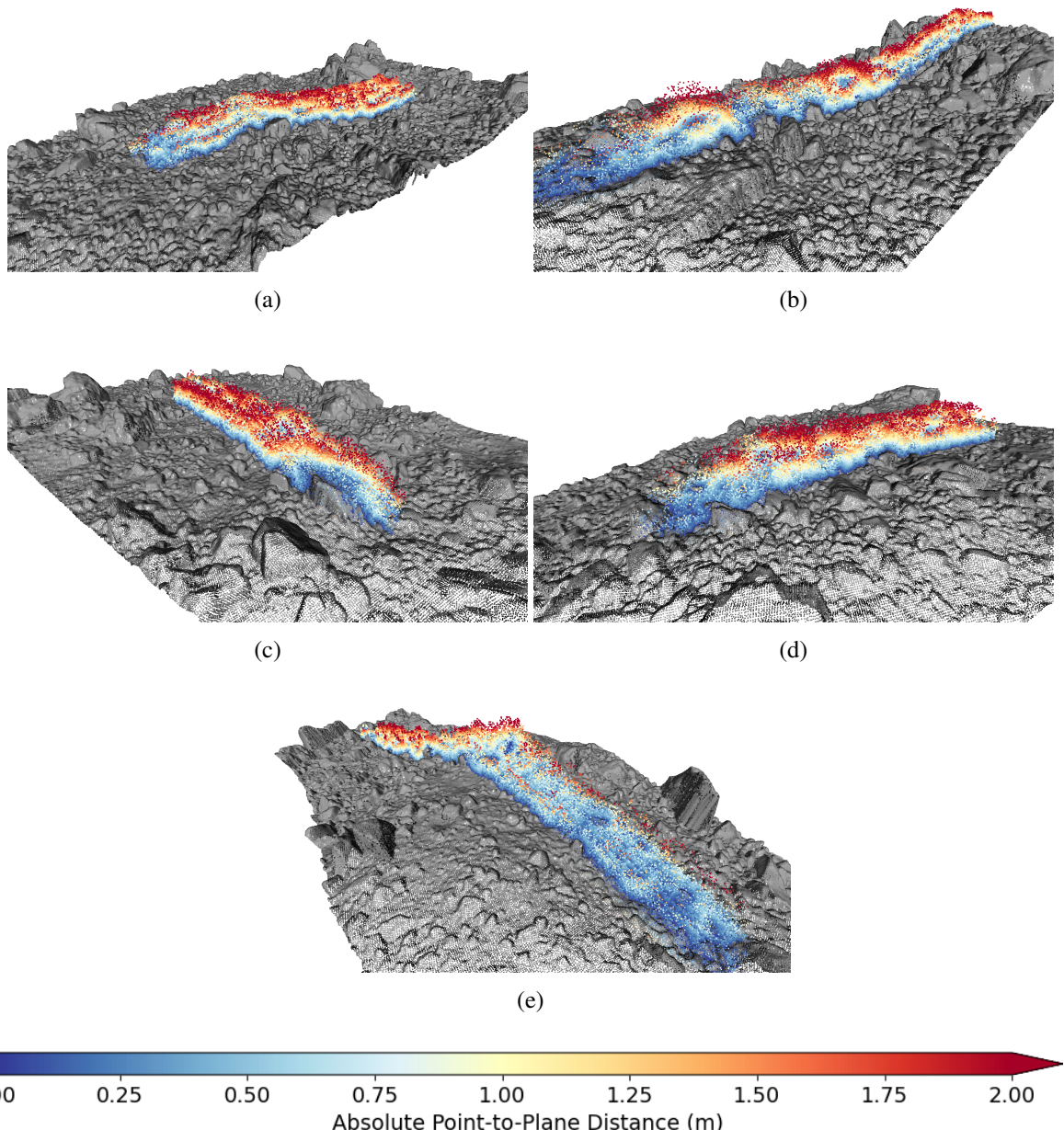


Figure 10: GNC-1 LIDAR fitted point cloud nearest neighbor point-to-plane distance errors: (a) Scan 1; (b) Scan 2; (c) Scan 3; (d) Scan 4; and (e) Scan 5.

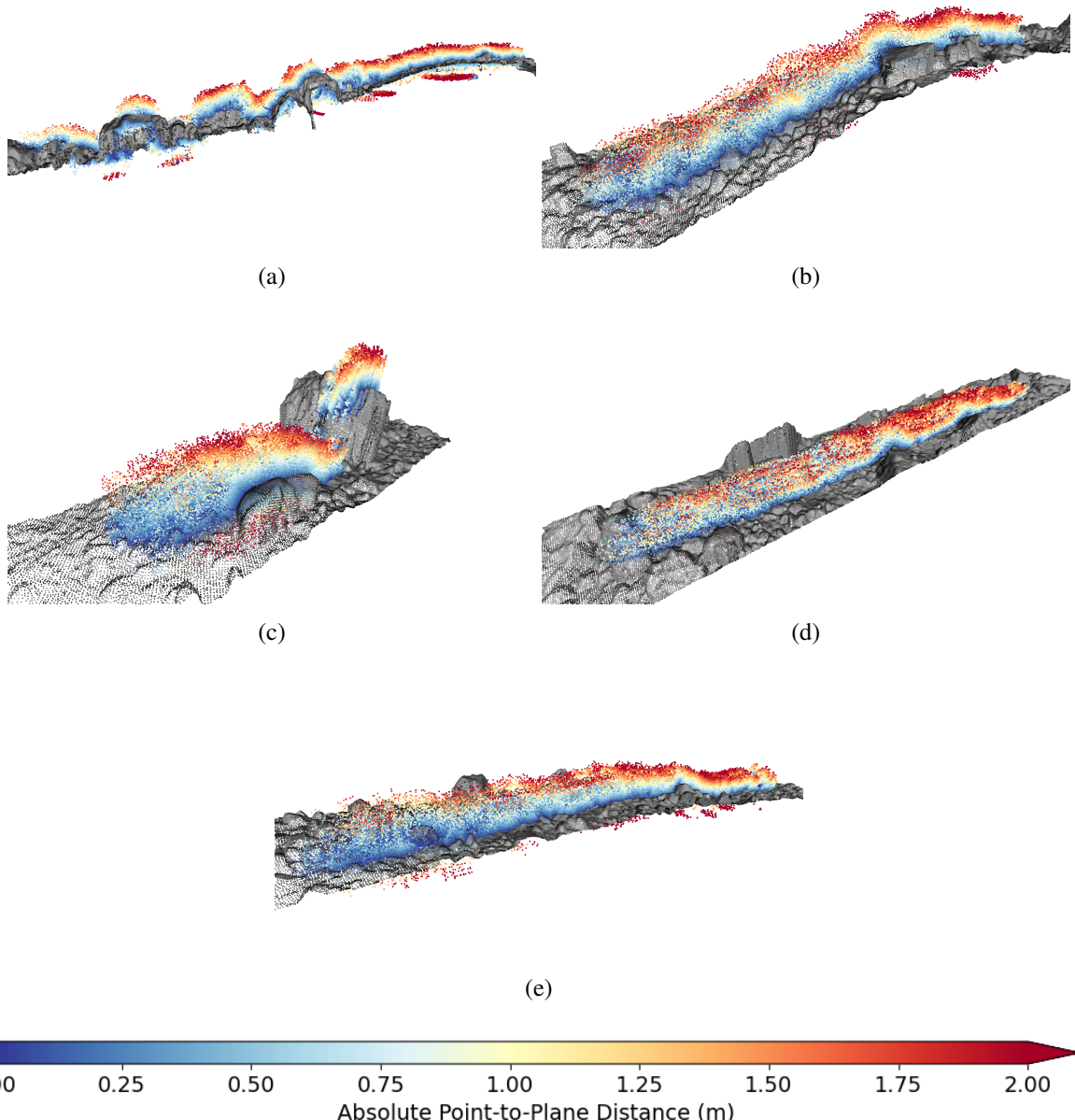


Figure 11: GNC-2 LIDAR fitted point cloud nearest neighbor point-to-plane distance errors: (a) Scan 1; (b) Scan 2; (c) Scan 3; (d) Scan 4; and (e) Scan 5.

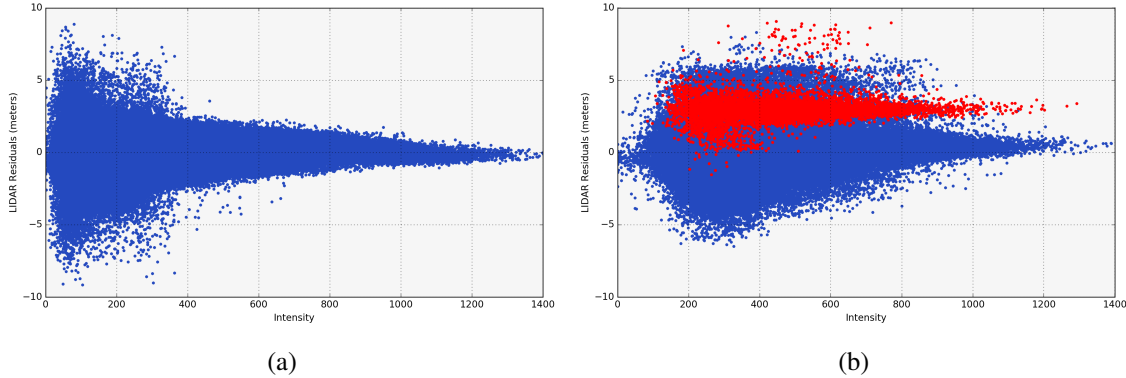


Figure 12: GNC LIDAR fitted residuals vs. intensity for all five scans of (a) GNC-1 LIDAR and (b) GNC-2 LIDAR where red indicates images with the 2.9 meter range jump.

Registration of GNC LIDAR Raw Image Ray-Traced Surface Intercept Model

The fitted GNC LIDAR raw image residuals based on the ray-traced surface intercept model were compared to the returned intensity (Figure 12) and the range-to-surface (Figure 13). The data used in this analysis did not filter based on intensity value, but outliers greater than 10 m were omitted.

The returned ranges in both GNC LIDARs were acquired over a range of intensities varying from 0 to 1400. Figure 12a shows the GNC-1 LIDAR range residuals vs. the returned intensity, while Figure 12b shows the GNC-2 LIDAR range residuals vs. the returned intensity. Both GNC LIDARs show a nearly linear reduction in noise as the intensity increases past 400 (un-filtered data used 500 as the minimum cutoff) with residuals less than 400 having an exponential increase in noise. GNC-2 LIDAR does show the 2.9 meter range bias occurring over all returned intensity values, indicating that this is most likely a bias induced by the instrument computation of the duration of the return. Figure 12b shows an increased noise structure near +5 m not associated with the 2.9 meter range jump. This increased noise is primarily due to the noise associated with GNC-2 Scan 1 and 3 seen in Figures 11a and 11c.

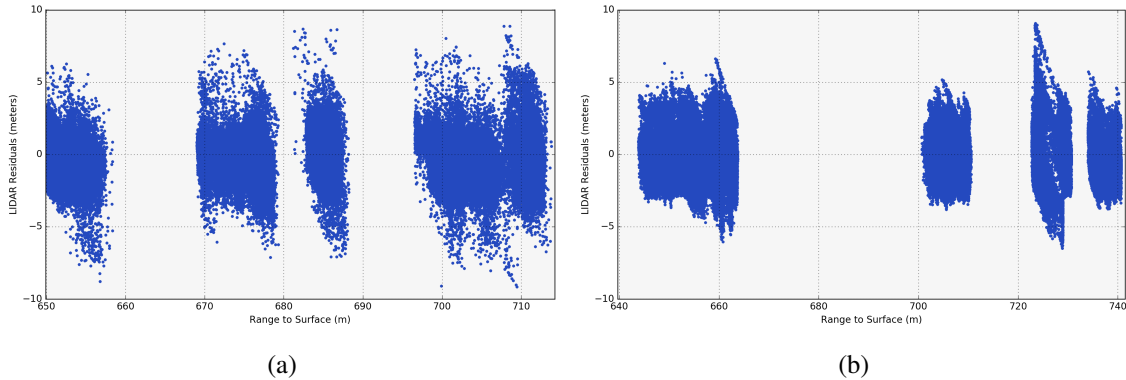


Figure 13: GNC LIDAR fitted residuals vs. the range to the surface for all five scans of GNC-1 LIDAR (a) and GNC-2 LIDAR (b).

GNC-1 and GNC-2 LIDARs range-to-surface varied between 645 m to 740 m throughout the five scans performed. Based on the requirements of the GNC LIDARs, this variation in range-to-surface should produce a potential mean and SD increase of about 1 m 3-sigma. Figure 13 shows the range-to-surface vs. the LIDAR range residual over this span of ranges. No appreciable increase in noise is seen over this range of altitudes the scans were performed at.

CONCLUSION

The OSIRIS-REx mission carried two distinct LIDAR systems: A scanning LIDAR called OLA as part of the science payload, and a flash LIDAR system as part of the GNC subsystem to serve as a navigation sensor during TAG. This presented a unique opportunity to compare the performance of the two LIDAR systems in proximity to a small asteroid body.

During the Orbital B mission phase, between June to August 2019, the OSIRIS-REx spacecraft orbited Bennu in a near-circular terminator orbit during which the altitude above the surface varied between 645 m to 740 m. Over a five week period observations were recorded with the OLA LEKT instrument that were subsequently used to construct a global DTM with a resolution of 5 cm and accuracy of ± 20 cm. This model provides an excellent reference for assessing the performance of the GNC LIDAR system. Two different GNC LIDAR checkout activities were also conducted during the Orbital B phase. A limb-crossing checkout featured a series of slews to collect GNC LIDAR data across varying ranges and phase angles and operate the AGC modes of the device. An OLA-GNC LIDAR cross calibration was designed to collect data from both the OLA and GNC LIDAR devices with overlapping footprints while the spacecraft was pointed nadir. This paper presented results from the OLA-GNC LIDAR cross calibration.

Point clouds generated from OLA measurements matched the underlying OLA-based DTMs to within 10 cm. GNC LIDAR measurements were compared to the OLA-based DTM and to OLA point clouds. Both the precision and accuracy of the GNC LIDAR were found to be significantly below the specified requirements, which include an error term that is equal to 1% of range. Precision of the GNC-1 LIDAR data was less than 0.9 m across the five observing periods. GNC-2 LIDAR data precision was less than 1.6 m. Utilizing methods to register GNC LIDAR point clouds to the underlying DTMs and remove major outliers, reported ranges were found to be consistent with the underlying topography within 1-2 meters. Noise levels in the GNC LIDAR data made it difficult to detect small topographic features in the point clouds. Predictably, the GNC LIDAR measurement noise was found to be proportional to return signal intensity, with intensity values below 400 being exponentially noisier. Notably GNC-2 LIDAR was found to exhibit range jumps of approximately 2.9 meters across all of the data sets; however, even with these range jumps the measured ranges were within specified requirements.

ACKNOWLEDGMENT

The authors acknowledge members of the entire OSIRIS-REx team including members of the Flight Dynamics System orbit determination, trajectory and maneuver design, and optical navigation sub-teams, the University of Arizona science planning and operations team, the Lockheed Martin flight operations team, and members of the Altimetry Working Group.

This material is based upon work supported by NASA under Contracts NNM10AA11C, NNG13-FC02C, and NNG12FD66C. OSIRIS-REx is the third mission in NASA's New Frontiers Program. Dante Lauretta of the University of Arizona, Tucson, is the principal investigator, and the University

of Arizona also leads the science team and the science observation planning and data processing. Lockheed Martin Space Systems in Denver built the spacecraft and is providing flight operations. Goddard Space Flight Center and KinetX Aerospace are responsible for navigating the OSIRIS-REx spacecraft.

LIST OF ACRONYMS

OSIRIS-REx Origins, Spectral Interpretation, Resource Identification, and Security–Regolith Explorer

TAG Touch-and-Go

OpNav Optical Navigation

OLA OSIRIS-REx Laser Altimeter

HELT High-Energy Laser Transmitter

LELT Low-Energy Laser Transmitter

LIDAR light detection and ranging

GNC Guidance, Navigation, & Control

NESC NASA Engineering and Safety Center

ICP Iterative Closest Point

AGC Automatic Gain Control

SSB Solar System Barycenter

REFERENCES

- [1] D. Lauretta, A. Bartels, M. Barucci, E. Bierhaus, R. Binzel, W. Bottke, H. Campins, S. Chesley, B. Clark, B. Clark, *et al.*, “The OSIRIS-REx target asteroid (101955) Bennu: Constraints on its physical, geological, and dynamical nature from astronomical observations,” *Meteoritics & Planetary Science*, Vol. 50, No. 4, 2015, pp. 834–849.
- [2] D. Lauretta, S. Balram-Knutson, E. Beshore, W. V. Boynton, C. D. d’Aubigny, D. DellaGiustina, H. Enos, D. Golish, C. Hergenrother, E. Howell, *et al.*, “OSIRIS-REx: sample return from asteroid (101955) Bennu,” *Space Science Reviews*, Vol. 212, No. 1-2, 2017, pp. 925–984.

- [3] D. S. Lauretta, H. L. Enos, A. T. Polit, H. L. Roper, and C. W. Wolner, “Chapter 8 - OSIRIS-REx at Bennu: Overcoming challenges to collect a sample of the early Solar System,” *Sample Return Missions* (A. Longobardo, ed.), pp. 163–194, Elsevier, 2021.
- [4] M. G. Daly, O. S. Barnouin, C. Dickinson, J. Seabrook, C. L. Johnson, G. Cunningham, T. Haltigin, D. Gaudreau, C. Brunet, I. Aslam, A. Taylor, E. B. Bierhaus, W. Boynton, M. Nolan, and D. S. Lauretta, “The OSIRIS-REx Laser Altimeter (OLA) Investigation and Instrument,” *Space Science Reviews*, Vol. 212, 2017, pp. 899–924.
- [5] O. Barnouin, M. Daly, E. Palmer, C. Johnson, R. Gaskell, M. Al Asad, E. Bierhaus, K. Craft, C. Ernst, R. Espiritu, *et al.*, “Digital terrain mapping by the OSIRIS-REx mission,” *Planetary and Space Science*, Vol. 180, 2020, p. 104764.
- [6] M. G. Daly, O. S. Barnouin, J. A. Seabrook, J. Roberts, C. Dickinson, K. J. Walsh, E. R. Jawin, E. E. Palmer, R. Gaskell, J. Weirich, T. Haltigin, D. Gaudreau, C. Brunet, G. Cunningham, P. Michel, Y. Zhang, R.-L. Ballouz, G. Neumann, M. E. Perry, L. Philpott, M. M. A. Asad, C. L. Johnson, C. D. Adam, J. M. Leonard, J. L. Geeraert, K. Getzandanner, M. C. Nolan, R. T. Daly, E. B. Bierhaus, E. Mazarico, B. Rozitis, A. J. Ryan, D. N. DellaGiustina, B. Rizk, H. C. M. Susorney, H. L. Enos, and D. S. Lauretta, “Hemispherical differences in the shape and topography of asteroid (101955) Bennu,” *Science Advances*, Vol. 6, No. 41, 2020.
- [7] J. A. Seabrook, M. G. Daly, O. S. Barnouin, C. L. Johnson, A. H. Nair, E. B. Bierhaus, W. Boynton, R. C. Espiritu, R. W. Gaskell, E. Palmer, L. Nguyen, M. Nolan, and D. S. Lauretta, “Global shape modeling using the OSIRIS-REx scanning Laser Altimeter,” *Planetary and Space Science*, Vol. 177, 2019, p. 104688.
- [8] K. Berry, P. Antreasian, M. C. Moreau, A. May, and B. Sutter, “OSIRIS-REx Touch and Go (TAG) Navigation Performance,” *38th Guidance and Control Conference*, No. AAS 15-125, Breckenridge, CO, American Astronautical Society, 2015.
- [9] O. Walther and K. Mahoney, “Bennu Asteroid Proximity Operations Navigation Using a Luenberger Observer with Flash LIDAR Range Measurements,” *38th Guidance and Control Conference*, No. AAS 15-116, Breckenridge, CO, American Astronautical Society, 2015.
- [10] K. Berry, K. Getzandanner, M. Moreau, P. Antreasian, A. Polit, M. Nolan, H. Enos, and D. Lauretta, “Revisiting OSIRIS-REx Touch-and-Go (TAG) Performance Given the Realities of Asteroid Bennu,” *43rd Guidance and Control Conference*, No. AAS 20-088, Breckenridge, CO, American Astronautical Society, 2020.
- [11] D. S. Lauretta, D. N. DellaGiustina, C. A. Bennett, D. R. Golish, K. J. Becker, S. S. Balram-Knutson, O. S. Barnouin, T. L. Becker, W. F. Bottke, W. V. Boynton, H. Campins, B. E. Clark, H. C. Connolly, C. Y. Drouet d’Aubigny, J. P. Dworkin, J. P. Emery, H. L. Enos, V. E. Hamilton, C. W. Hergenrother, E. S. Howell, M. R. M. Izawa, H. H. Kaplan, M. C. Nolan, B. Rizk, H. L. Roper, D. J. Scheeres, P. H. Smith, K. J. Walsh, C. W. V. Wolner, and The OSIRIS-REx Team, “The unexpected surface of asteroid (101955) Bennu,” *Nature*, Vol. 568, No. 7750, 2019, pp. 55–60.
- [12] C. Miller, R. Olds, C. Norman, S. Gonzales, C. Mario, J. Leonard, and D. Lauretta, “On Orbit Evaluation of Natural Feature Tracking for OSIRIS-Rex Sample Collection,” *43rd Annual AAS Guidance and Control Conference*, No. AAS 20-148, Breckenridge, CO, 2020.
- [13] B. Bos, M. Ravine, M. Caplinger, J. Schaffner, J. Ladewig, R. Olds, C. Norman, D. Huish, M. Hughes, S. Anderson, D. Lorenz, A. May, C. Jackman, D. Nelson, M. Moreau, D. Kubitschek, K. Getzandanner, K. Gordon, and A. Eberhardt, “Touch And Go Camera System (TAGCAMS) for the OSIRIS-REx Asteroid Sample Return Mission,” *Space Science Reviews: The Origins, Spectral Interpretation, Resource Identification, Security - Regolith Explorer (OSIRIS-REx) Mission*, 2017.
- [14] E. Church, T. Bourbeau, J. Curriden, A. Deguzman, F. Jaen, H. Ma, K. Mahoney, C. Miller, B. Short, K. Waldorff, O. Walther, and D. Lauretta, “Flash Lidar On-Orbit Performance at Asteroid Bennu,” *43rd Annual AAS Guidance and Control Conference*, Breckenridge, CO, 2020, AAS 20-148.
- [15] J. A. Christian and S. Cryan, “A Survey of LIDAR Technology and its Use in Spacecraft Relative Navigation,” *AIAA Guidance, Navigation, and Control (GNC) Conference*, Boston, MA.
- [16] R. Richards, J. Tripp, S. Pashin, D. King, J. Bolger, and M. Nimelman, “Advances in Autonomous Orbital Rendezvous Technology: The XSS-11 Lidar Sensor,” *57th IAC/IAF/IAA (International Astronautical Congress)*, Valencia, Spain, Oct 2006.
- [17] J. Whiteway, M. Daly, A. Carswell, T. Duck, C. Dickinson, L. Komguem, and C. Cook, “Lidar on the Phoenix mission to Mars,” *Journal of Geophysical Research: Planets*, Vol. 113, No. E3, 2008.
- [18] N. Dennehy, P. Parker, S. Cryan, F. Clark, J. Christian, J. Valdez, A. Heaton, M. Patangan, G. Spiers, M. Strube, and D. Brown, “Relative Navigation Light Detection and Ranging (LIDAR) Sensor Development Test Objective (DTO) Performance Verification,” Technical Memorandum (TM) NESC T1-11-00753, NASA Langley Research Center, Hampton, VA, United States, May 2013.

- [19] T. D. Moyer, *Formulation for observed and computed values of Deep Space Network data types for navigation*, Vol. 3. John Wiley & Sons, 2005.
- [20] W. M. Owen Jr, “Methods of optical navigation,” No. AAS, 2011.
- [21] S. Urban and P. Seidelmann, *Explanatory Supplement to the Astronomical Almanac*. University Science Books, 2012.
- [22] M. H. Soffel and W.-B. Han, “Applied General Relativity,” *Astronomy and Astrophysics Library. Springer Nature Switzerland, Cham*, 2019.
- [23] W. J. Riley, *Handbook of frequency stability analysis*. US Department of Commerce, National Institute of Standards and Technology, 2008.
- [24] M. Sorrel and R. Langhans, “Space-time reference systems,” 2013.
- [25] D. Rowlands, D. Pavlis, F. Lemoine, G. Neumann, and S. Luthcke, “The use of laser altimetry in the orbit and attitude determination of Mars Global Surveyor,” *Geophysical Research Letters*, Vol. 26, No. 9, 1999, pp. 1191–1194.
- [26] E. Mazarico, G. Neumann, D. Rowlands, and D. Smith, “Geodetic constraints from multi-beam laser altimeter crossovers,” *Journal of Geodesy*, Vol. 84, No. 6, 2010, pp. 343–354.
- [27] H. Xiao, A. Stark, G. Steinbrügge, H. Hussmann, and J. Oberst, “Processing of laser altimeter time-of-flight measurements to geodetic coordinates,” *Journal of Geodesy*, Vol. 95, No. 2, 2021, pp. 1–23.
- [28] S. Goossens, D. D. Rowlands, E. Mazarico, A. J. Liounis, J. L. Small, D. E. Highsmith, J. C. Swenson, J. R. Lychkoft, B. W. Ashman, K. M. Getzandanner, *et al.*, “Mass and shape determination of (101955) Bennu using differenced data from multiple OSIRIS-REx mission phases,” *The Planetary Science Journal*, Vol. 2, No. 6, 2021, p. 219.
- [29] D. Farnocchia, S. R. Chesley, Y. Takahashi, B. Rozitis, D. Vokrouhlický, B. P. Rush, N. Mastrodemos, B. M. Kennedy, R. S. Park, J. Bellerose, D. P. Lubey, D. Velez, A. B. Davis, J. P. Emery, J. M. Leonard, J. Geeraert, P. G. Antreasian, and D. S. Lauretta, “Ephemeris and hazard assessment for near-Earth asteroid (101955) Bennu based on OSIRIS-REx data,” *Icarus*, Vol. 369, 2021, p. 114594.
- [30] A. Savitzky and M. J. Golay, “Smoothing and differentiation of data by simplified least squares procedures.,” *Analytical chemistry*, Vol. 36, No. 8, 1964, pp. 1627–1639.
- [31] P. Babin, P. Giguere, and F. Pomerleau, “Analysis of robust functions for registration algorithms,” *2019 International Conference on Robotics and Automation (ICRA)*, IEEE, 2019, pp. 1451–1457.